LA-UR-18-21099 (Accepted Manuscript)

Structure/property (constitutive and spallation response) of additively manufactured 316L stainless steel

Gray, George Thompson III
Livescu, Veronica
Rigg, Paulo
Trujillo, Carl Patrick
Cady, Carl Mcelhinney
Chen, Shuh-Rong
Carpenter, John S.
Lienert, Thomas J.
Fensin, Saryu Jindal

To be published in: Acta Materialia

DOI to publisher's version: 10.1016/j.actamat.2017.07.045

Permalink to record: http://permalink.lanl.gov/object/view?what=info:lanl-repo/lareport/LA-UR-18-21099

Structure / Property (Constitutive and Spallation Response) of Additively Manufactured 316L Stainless Steel

G.T. Gray III[1], V. Livescu[1], P.A. Rigg[2], C.P. Trujillo[1], C.M. Cady[1], S.R. Chen[1], J.S. Carpenter[1], T.J. Lienert[1], S.J. Fensin[1]

[1]Los Alamos National Laboratory, Los Alamos, New Mexico, 87545, USA
[2]Institute for Shock Physics, Washington State University, Pullman, Washington, 99164, USA

Abstract.

For additive manufacturing (AM) of metallic materials, the certification and qualification paradigm needs to evolve as there is currently no broadly accepted "ASTM- or DIN-type" additive manufacturing certification process or AM-produced material specifications. Accordingly, design, manufacture, and subsequent implementation and insertion of AM materials to meet engineering applications requires detailed quantification of the constitutive (strength and damage) properties of these evolving materials, across the spectrum of metallic AM methods, in comparison/contrast to conventionally-manufactured metals and alloys. For this study, cylindrical samples of 316L SS were produced using a LENS MR-7 laser additive manufacturing system from Optomec (Albuquerque, NM) equipped with a 1kW Yb-fiber laser. The microstructure of the AM-316L SS was characterized in both the "as-built" AM state and following a heat-treatment designed to obtain full recrystallization to facilitate comparison with annealed wrought 316L SS. The constitutive behavior as a function of strain rate and temperature was characterized and is compared to that of annealed wrought 316L SS plate material. The dynamic shock-loading-induced damage evolution and failure response of all three 316L SS materials was quantified using flyer-plate impact driven spallation experiments at peak stresses of 4.7 and 6.5 GPa. The spall strength of AM-produced 316L SS and the recrystallized-AM-316L SS were found to decrease with increasing peak shock stress while the annealed wrought 316L SS spall strength remained essentially constant. The damage evolution, characterized using optical metallography and electron-backscatter diffraction (EBSD), was found to vary significantly across the three 316L SS microstructures while the three samples loaded to a peak shock stress of 6.5 GPa displayed only ~12% differences in spall strength.

Keywords:

Additive Manufacturing, 316L SS, spallation, microstructure, damage evolution

1. Introduction

Additive manufacturing (AM) is a rapidly evolving technology fueling revolutionary transformations in rapid prototyping, freeform, and net-shape manufacturing. Driving this is the ability to locally produce singular or high-value, low-volume manufactured parts or components[1, 2]. Several recent extensive reviews have surveyed the state-of-the-art of metal additive technologies [1-4]. The AM of metallic components offers opportunities for increased efficiencies in energy, cost, and time savings during manufacturing[1, 5-14]. Conversely, AM production of metallic components must be scoped within the caveats of the relatively high expense of AM machines, high feedstock costs, limited build volumes, slow deposition rates, and evolving certification / qualification procedures / requirements for high-consequence applications[1, 4]. Further, a lack of systematically quantified processing / structure / properties / performance (PSPP) data, due to published research too often failing to document detailed specifics of: 1) feedstock pedigree, 2) detailed AM machine processing settings, 3) quantified component / build thermal histories, 4) detailed build-orientation-mechanical testing property correlations, and 5) detailed microstructure / texture and defect statistics, each hampers efforts to develop a rigorous roadmap to certifying / qualifying AM metals and alloys.

In addition, for AM materials or components to supplant conventional manufactured materials and processes, assuming the performance requirements are met, the certification and qualification paradigm needs to evolve as there exists no universally-accepted "ASTM-type" additive manufacturing certification process or generic AM-material produced specifications. In fact, given the range of microstructural spectrum possible between powder-bed fusion, directed energy deposition, binder jetting, and sheet lamination AM technologies[1, 4] for a given metal or alloy, a generic AM metal or alloy specification disconnected from its AM technology appears highly unlikely. Even for minor changes in starting feed material (powder or wire), component geometry, build process variables, and post-build thermo-mechanical processing, the qualification cycle can be complicated leading to long implementation times. This is due in large part to the fact that we are not able to predict and control PSPP relationships[1, 4, 15-17]. Metal or alloy-component certification requirements have been discussed elsewhere[1, 4] in the case of some manufacturing processes but generally involve meeting engineering and physics requirements tied to the specific narrow functional constraints of the engineering component and finally process and product qualification. For AM materials and components to meet broader metal or alloy-based qualification and certification requirements for critical engineering applications, key microstructural parameters and defects must be quantified and quantitatively linked to the specific AM processing and equipment parameters to establish minimum performance properties[1, 4, 18]. Further, while there is a growing number of detailed structure-property studies of AM materials subjected to quasi-static and/or fatigue loading stress states, there remains to date few studies systematically quantifying their behavior at higher strain rates, shock loading, and/or when subjected to dynamic tensile 1D spallation loading[19, 20].

316L stainless steel(hereafter 316L SS) is a quotidian austenitic SS that sees widespread usage in marine, energy, aerospace, and medical environments because of its combination of strength and corrosion resistance. The pervasiveness of its usage and wide availability of relatively inexpensive feedstock for AM, has led to several recent publications that focus on the structure-property behavior of this particular alloy system[21-26]. These studies have strived to quantify the connections between defects, such as porosity, lack of powder melting, and surface defects, and then link these flaws with performance when subjected to standard mechanical behavior tests[21, 23]. Although structure-property data of this type is important in qualifying

AM products, a major concern remains when comparing AM parts with those made using traditional metal manufacturing methods, in particular the failure and damage mechanisms that arise from the unique microstructures produced during AM[4, 27]. A number of studies exist in the area of high cycle fatigue that begin to make such connections between AM microstructures and damage evolution and failure[1, 4, 28, 29] but none to date have probed the dynamic damage evolution in the 316 stainless steel series. Further, no studies of the damage evolution due to shock spallation loading as a function of peak shock stress of an AM-produced 316L SS material has been conducted to date[30]. Dynamic damage resistance is of relevance to utilization of potential future application of AM materials in high-rate manufacturing (forging or machining), crashworthiness (aerospace and automotive), and defense applications[31]. The purpose of this paper is to report constitutive and shock-loading-induced dynamic fracture (spallation) properties as a function of various peak shock stresses of 316L SS produced by Laser Engineered Net Shaping (LENS) additive manufacturing in comparison to annealed wrought 316L SS and AM-316L SS following recrystallization. Section 2 of this paper discusses the details of the plate-impact experiments and resulting analysis undertaken in this study. The results and conclusions are presented in Sections 3 and 4, respectively.

2. Experimental Procedure

2.1 Material & Additive Manufacturing Processing

This study involved production, microstructural characterization, quasi-static and dynamic compression testing, and shock-induced spallation testing of solid cylinders of 316L austenitic stainless steel produced by LENS additive manufacturing[11, 12] and compared with wrought 316L SS plate. The wrought 316L SS was procured in 12.5 mm-thick plate form. The 316L powder was gas-atomized powder procured from Carpenter Powder Products (Bridgewater, PA). The analyzed chemical composition of the wrought annealed 316L SS plate and the 316L SS powder utilized in the LENS builds is presented in Table I. An inert gas fusion method (ASTM E 1019-11) was used to determine the wt.% oxygen for the powder (0.013 wt. %) and in the LENS as-built cylinders (0.018 wt. %). The powder particle size distribution was measured to be -80/+270 mesh (53 μm to 180 μm) and was quantified using standard metal powder sieve analysis.

Table I: Chemical Analysis of Annealed Wrought 316L SS plate and 316L SS Powder

Wt. %	**C**	**Cr**	**Cu**	**Mn**	**Mo**	**N**	**Ni**	**P**	**S**	**Si**
Wrought	0.022	16.16	0.39	1.70	2.08	0.063	10.03	0.029	0.0004	0.40
Powder	0.02	20.7	0.19	1.32	2.45	0.09	11.4	0.02	0.01	0.50

Right-regular cylinders of 316L SS, were produced using a LENS MR-7 laser AM system from Optomec (Albuquerque, NM) equipped with a 1kW Yb-fiber laser. The laser beam was delivered to the collimator through a 200 μm stepped-index-fiber optic and was focused via a lens with a focus length of 160.4 mm at 1070 nm wavelength of the fiber laser. The laser focus condition was positioned so that the minimum waist of the focused beam was located ~3.8 mm below the substrate surface. The measured laser power employed throughout the trials was 380 W. The laser beam was directed normal to the substrate and passed through a nozzle ~20 mm in

diameter accompanied by an argon shield gas with a flow rate of 20 lpm to prevent damage to the optics.

Powder was delivered to the deposition region through four nozzles with exit orifices positioned concentrically around the larger nozzle. The exit orifices of the nozzles were positioned approximately 9.5 mm above the substrate surface. The four nozzles were arranged symmetrically about the laser beam axis and were angled downward toward the substrate at ~25 degrees. The powder delivery system incorporated a screw feed mechanism operated at 3.5 revolutions per minute (RPM) with an argon gas flow rate of 5 liters per minute (lpm) of argon gas for the deposit. A mass flow rate of the 316L SS powder of ~6.3 $gm \cdot min^{-1}$ was determined with these settings by averaging three measurements conducted by capturing powder for one minute intervals from the nozzles in a plastic bag.

The AM components produced were solid cylinders 2.5 cm in diameter and 3.3 cm tall. The cylinder was deposited onto a substrate comprised of a 0.95 cm thick plate of 304L SS. A "z" step height of 0.30 mm was used with a hatch spacing of 0.46 mm. Each layer was produced using linear "hatching" passes at 1.12 cm s^{-1}. The direction of the hatching passes was alternated between 0°, 90°, 180° and 270° directions before repeating. Oxygen levels were monitored throughout the AM build and did not exceed 6 ppm at any point.

After AM fabrication, the 304L substrates were machined away. Several cylinders were sectioned to provide AM-as-built samples while others were heat-treated to recrystallize the AM microstructure. The recrystallization heat treatment was 1060°C for one hour under vacuum followed by cooling to room temperature in 2 ½ minutes by rapid Argon gas quenching. The heat treatment led to a fully recrystallized AM microstructure (hereafter referred to as AM-Rx or AM-recrystallized).

2.2 Microstructure / Post-Mortem Characterization

Electron backscatter diffraction (EBSD)[32] and light optical microscopy (LOM) were utilized to investigate the cross-sections of the three starting 316L SS materials as well as sections from the incipiently spalled samples following shock recovery. Sample preparation consisted of grinding on SiC paper with increasingly finer grit, followed by mechanical polishing with 0.3 μm alpha alumina slurry and then a mixture of 5:1 by volume of 0.04μm colloidal silica and hydrogen peroxide. Optical microscopy images were acquired at various magnifications using a Zeiss Axio Imager M2m optical microscope of the starting microstructures and those following incipient spallation testing. In preparation for EBSD analysis, the samples were electropolished and very slightly electro-etched in a solution of 60% nitric acid and 40% water, at 6V and 3V, respectively. EBSD analysis was performed with a step size of 0.25 μm on a Phillips XL30 FEG SEM, using the TSL Data Collection and Analysis software.

EBSD crystal direction maps of the microstructures of the three 316L SS starting materials are shown in Figure 1. The EBSD scans were performed in the in-plane direction for the three materials. The annealed wrought plate material exhibits an equiaxed microstructure displaying a nominal average grain size of 29 μm. The crystallographic texture of this 316L SS was investigated using X-ray diffraction to be almost random [33, 34]. The AM-As-Built displays a macroscopic squamous or fish-scale type morphology optically (see LOM insert) indicative of the deposit interfaces of the alternate layers of the build and a complex, fine-scaled, and dendritic microstructure with an average grain size of 4.5 μm. The as-deposited microstructure is characterized by a primary matrix of austenite (FCC) with 2-2.5 volume % ferrite (BCC), based

on EBSD analysis and magnetometer measurements, due to the primary solidification to ferrite[35]. The AM-Rx displayed a nominally polycrystalline microstructure albeit coarser and less faceted than the equiaxed microstructure of the wrought 316L SS with an average grain size of 59 μm. The texture of the three microstructures shown in Figure 1, expressed in multiples of random (MRD), was very similar with intensities of 2MRD, 2.7MRD, and 2.6MRD.

An estimate of the extent of damage evolution across the major diameter of the cross-sectioned incipiently- spalled samples was characterized from analysis of the void formation based on LOM micrographs. Void diameter and number in each sample was determined using ImageJ Software[36]. Spherical voids were assumed when calculating the average void diameter and void volume fraction. Each image was converted to greyscale and then a threshold applied so that voids were selected but other dark features such as grain boundaries were not. The selected voids were then subjected to a particle size analysis to calculate the void number, size, and area percentage.

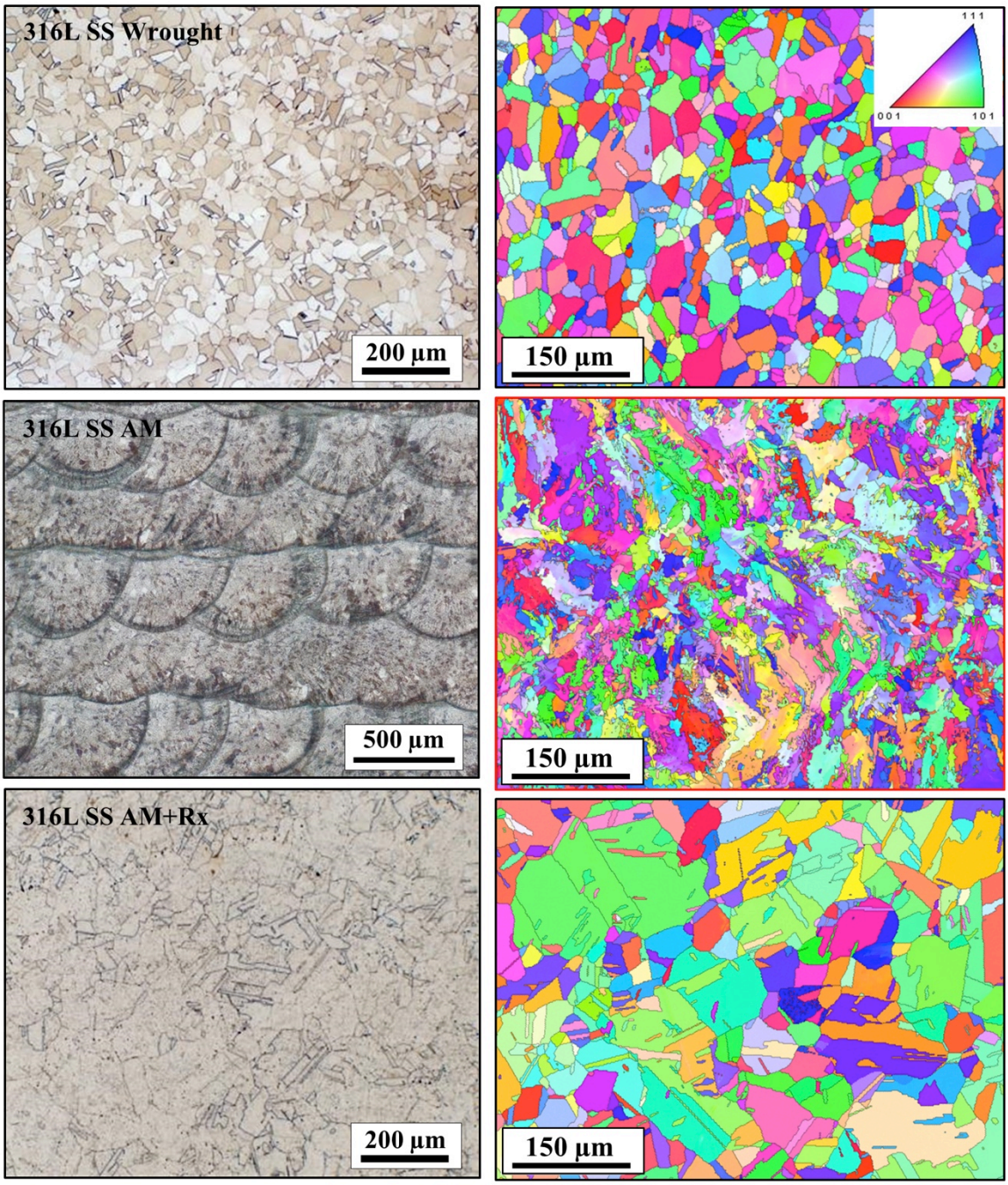

Fig. 1. Light Optical Microscopy (left) and Electron-Back-Scatter Diffraction (right) images of the 316L SS materials studied: top: annealed wrought plate, middle: AM-(As-Built), and bottom: AM-following recrystallization heat-treatment at 1060C for 1 hour (AM-Rx).

2.3 Constitutive / Spallation Testing

Cylindrical samples were electro-discharge machined to dimensions of 5 mm in height and 5 mm

in diameter for quasi-static and dynamic mechanical testing. The compression axis of these samples was parallel to the AM cylinder axis for the 316L SS AM and parallel to the thru-thickness plate direction for the 316L SS wrought. Quasi-static compression tests were conducted using an Instron screw-driven test system at a strain rate of 0.001 s^{-1} and temperature of 298 K, with $MoSi_2$ lubrication to minimize barreling. Strain-rate jump tests from 0.001 to 0.1 s^{-1} were conducted at 233K to assess the strain-rate sensitivity of the three 316L SS materials. Dynamic compression testing was conducted using a split-Hopkinson Pressure Bar (SHPB)[37]. The SHPB samples were similarly lubricated using $MoSi_2$ to minimize friction at the sample-pressure bar interfaces[37].

Spallation experiments were performed on an 80-mm single-stage gas gun[38] using the configuration shown in Fig. 2. Impactors of wrought 316L SS were accelerated at velocities of 257 and 350 m/s and impacted onto the 316L SS targets to achieve peak shock stresses of 4.7 and 6.5 GPa, respectively. To assure an identical shock stress-time history for all three samples, each of the three 316L SS materials were placed in a single shock spall assembly as seen in Figure 2. In the experiment, the impactor thickness (2.5 mm) was kept at one-half the sample thickness (5 mm) to cause tensile damage to occur in the center of the sample thickness. Each target consisted of three separate components: a target plate, three samples, and a momentum ring surrounding each sample. The surrounding momentum trapping rings were made from wrought material with an inner diameter (ID) 0.1mm less than the outer diameter (OD) of the sample. The OD of the rings was 16.5 mm with the holes in the target plate made to 16.4mm diameter to accommodate press fitting of all parts. Spallation experiments, and "soft" recovery of the shocked samples using low-density foam and water baffles, were conducted following the nominal procedures as detailed previously[38]. For the three-sample targets, samples were machined as right circular cylinders 12.7 mm in diameter from the wrought, AM-as-built, and the AM-Rx 316L SS materials. The assembled targets were lapped flat and parallel to within 5 μm.

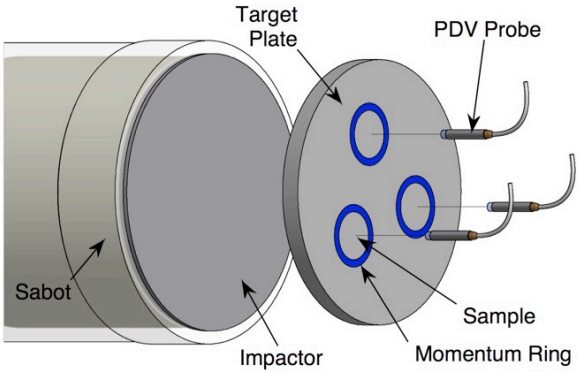

Fig. 2. Experimental configuration used to produce incipient damage or complete spall in the three 316L SS samples simultaneously. Wrought 316L SS impactors were accelerated in an 80 mm gas gun and impacted onto the target to produce the two peak shock stresses studied. PDV probes were positioned to view the center of each sample to provide free-surface velocimetry data from each of the three samples in each spallation experiment.

Samples were placed in the target ring such that the shortest distance between the sample edges to each other and to the edge of the target plate were equal. Free surface velocities were measured in each experiment using Photon Doppler Velocimetry (PDV) [39, 40]. Collimated probes procured from AC Photonics (Part #: 1CL15P020LC-C01) were positioned to collect

velocimetry data from the center of the rear of each sample and connected to a LANL-built 4-channel PDV system. One additional PDV probe (not shown in figure) was placed next to each target plate to measure the projectile velocity directly to an accuracy of 0.1%[40]. A single PZT trigger pin (Dynasen, Inc.) was also positioned next to each target plate with a typical standoff distance of a few millimeters to provide a trigger to the digitizer used to collect the PDV data.

3. Results and Discussion

3.1 Constitutive Response

The quasi-static and dynamic compressive constitutive response of the three 316L SS materials is shown in Fig. 3a and 3b. The as-built AM material quasi-statically exhibits nominally twice the yield strength of the additive material following recrystallization (AM-Rx) and ~60% higher compressive yield than the annealed wrought plate. Following yielding, all three 316L SS materials displayed similar rates of work hardening (work-hardening slopes). The SHPB data is seen to display similar trends in the flow stress exhibiting essentially identical stress-strain behavior for a nominal strain rate of 1200 / sec at 298K. The work-hardening rates for the AM-Rx and wrought materials are identical while the AM material shows a slightly lower rate of hardening although still displaying substantial hardening.

To evaluate if the substantially higher quasi-static flow stress levels in the AM-as-built material was principally dominated by a high starting dislocation density or level of residual stress versus the very fine dendritic substructure typical of AM materials[1], strain rate jump tests were conducted at 233 and 298K. The magnitude of increase in the flow stress with the strain rate jumps was seen to be invariant for all three materials; see the rate-jump insert in Fig. 3 conducted at 233K. The similarity in rate-jump response suggests the higher starting yield and flow stress displayed by the AM-as-built material is principally due to an intrinsic athermal barrier component to the strength[41] consistent with the extremely fine dendritic substructure, within the macroscopic “fish-scale” macrostructure, formed during the rapid solidification rates occurring in LENS builds, and not dominated by either a high starting defect population or residual stresses[42, 43]. The significant difference in the flow stress level in the AM-as-built 316L SS compared to the wrought or AM-Rx materials is further consistent with the known, pronounced Hall-Petch behavior of 316L SS where decreasing the grain size from 33 to 3 μm has been shown to increase the quasi-static yield strength by 50% at 297K[44].

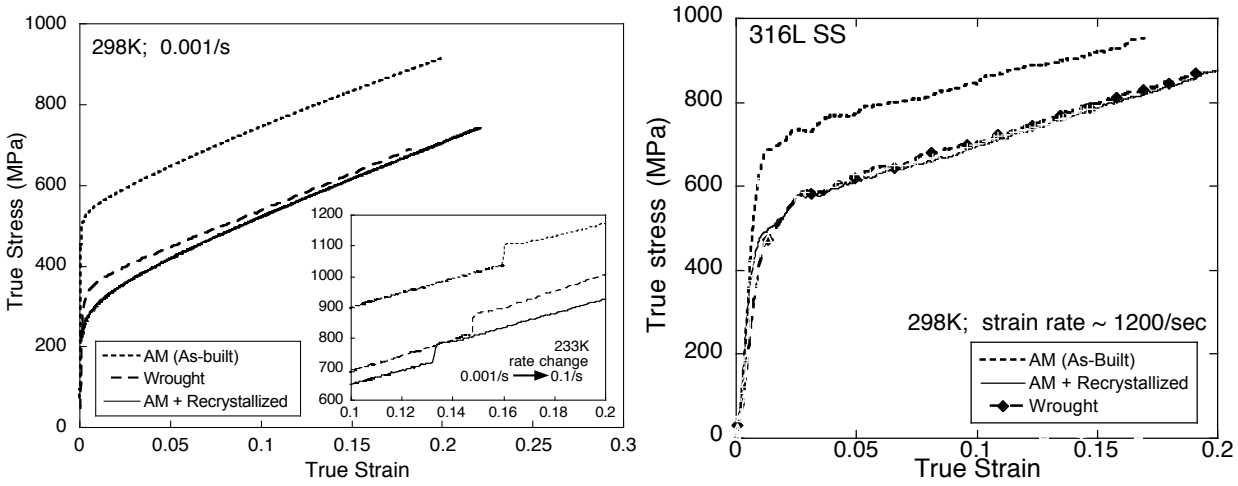

Fig. 3. Compressive a) quasi-static and b) dynamic SHPB, true stress-true strain responses of 316L SS in the AM-as-built condition, AM + recrystallization heat-treatment, and annealed wrought 316L SS.

To investigate the above hypothesis, Orientation Imaging Microscopy (OIM) from EBSD is ideal for the identification of the grains. In this study, we used the TSL Data analysis software[45] to not only analyze the grain size, but also to investigate the type of boundaries. Compared to the wrought and AM+Rx materials, the 316L SS AM microstructure exhibits a complex grain substructure. The average equivalent grain size measurement was performed using classical grain size analysis from multiple EBSD scans by imposing a grain tolerance angle of 5 degrees. This means that connected points with orientations within this angle tolerance were grouped into a grain. The grain size is then calculated as the diameter of the circle with the same area as that grain. Using this approach, the point-to-point misorientation within a grain will be small, but the spread of misorientation within a grain can be large, which works well for AM microstructures. The boundary type analysis concluded that the internal grain substructure is formed by regions misoriented at up to 2 degrees, therefore these regions were not considered to be separate grains. This analysis yields an average macroscopic grain size of 4.5 μm with a range of 2.5-60 μm. Please note that this measurement is performed on 2D sections and grain size interpretation must be done with care considering the complex morphology of the AM 316L. In this case, it only provides a simple comparison of grain scales among different materials from 2D sections. By superimposing an image quality map, the dendritic features become apparent as also shown in Figure 4. Careful measurements performed on optical images indicate that dendrite thickness is approximately 1.5-2.6μm. The difficulties in performing these measurements arise from the dendrites' complex morphology and from the 2D nature of observations in both the optical and EBSD analysis. However, it is the belief of the authors that these finer inter-dendritic dimensions are important to the overall mechanical behavior of the AM-as-built 316L SS and contribute to the Hall- Petch strengthening in the 316L AM material.

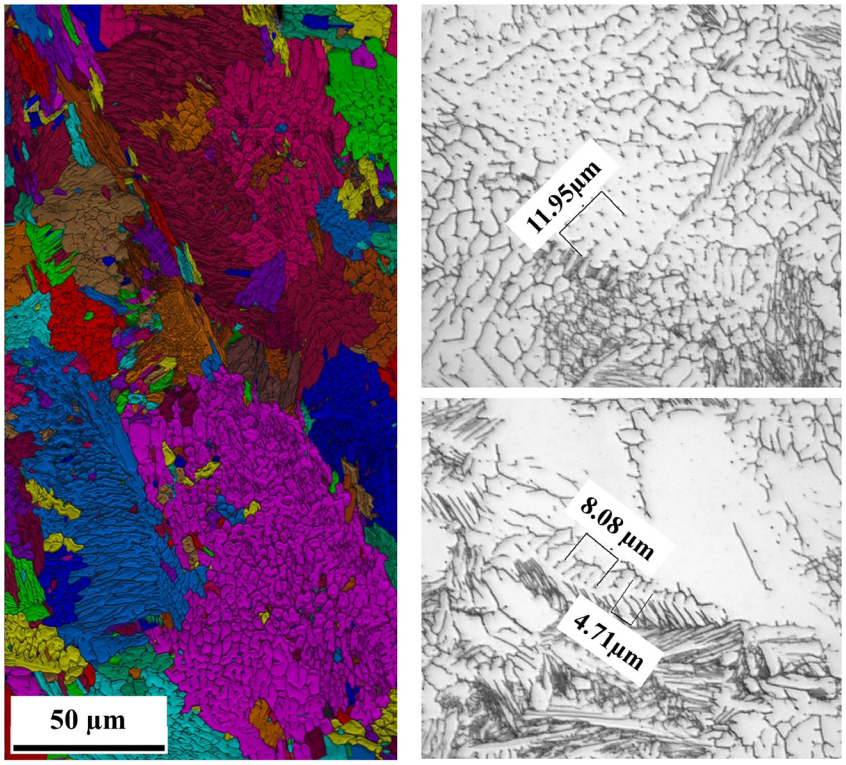

Fig. 4. 316L AM microstructure showing unique grain color map (left) and optical microscopy images dendritic spacing.

Cooling rates through the solidification range can be assessed from knowledge of dendrite arm spacing. The relationship between primary dendrite or cell spacing (d) and cooling rate (CR) has the form: $d = \alpha(CR)^{-n}$ where α is a material dependent constant and the exponent n~1/3 (no secondary dendrite arms)[46]. For austenitic stainless steels, values of α (80) and n (0.33) have been reported[47], where d has units of µm and CR has units of K s^{-1}. Another study reported values of 54 (α) and 0.32 (n) with the same units[48]. Estimates of cooling rates through the solidification range determined from primary dendrite spacing measurements on several micrographs indicated a cooling rate ranging from 5.5 x 10^3 K s^{-1} to 1.1 x 10^4 K s^{-1}.

The maximum cooling rate during solidification was also estimated using results of a top viewing, two-color pyrometer. In a separate experiment, the thermal gradient ($\underline{\mathbf{G}} = dT/dr_{s/l}$) at the center of the trailing edge of the melt pool for a similar stainless steel was measured at ~ 717 K mm^{-1} with the pyrometer. The cooling rate can be calculated using the dot product $\underline{\mathbf{G}} \bullet \underline{\mathbf{R}}$, where R is the solidification rate (mm s^{-1}). The maximum solidification rate occurs along the centerline of the melt pool and is assumed to be approximately equal to the travel rate. Using this procedure, a maximum cooling rate of ~ 8 x 10^3 K s^{-1} was calculated for the conditions used here. Note the good agreement with the dendrite spacing measurements discussed above.

3.2 Velocimetry

The peak particle velocities, U_p, ranged from 127-175 m/s, corresponding to peak compressive shock stresses of 4.65 – 6.52 GPa. These values are calculated using the measured impact velocity and the Mie Grüneisen equation of state for 316 SS: ρ_o = 7.96 gr/cm^3 (density), measured C_o= 4.474 (AM), 4.464 (AM-Rx) and 4.35 (wrought) mm/ms (bulk sound speed), s=1.54 and γ=2.17. The spall strength (σ_{spall}) is calculated using the relationship from Kanel[49] for a material that exhibits an elasto-plastic behavior:

$$\sigma_{spall} \equiv \rho_0 C_L \Delta FSV \left(1 + \frac{C_L}{C_o}\right)^{-1} \qquad \text{Eq. (1)}$$

where C_L = 5.73 (AM), 5.72 (AM-Rx) and 5.70 (wrought) mm/ms is the longitudinal sound speed and ΔFSV is the difference in the free surface velocity from the peak state to the minima in the pull-back in the U_p as measured by the PDV.

The free surface velocity data for the three 316L SS materials spallation experiments conducted at a impact velocities of 257 and 350 m/s are presented in Fig. 5a and 5b, for the 4.7 and 6.5 GPa peak stress shocks, respectively. In the 4.7 GPa experiment, Fig. 5a, the wave profiles for the three materials display (see labels on figure): 1) nominally similar elastic-plastic transitions, or Hugoniot Elastic Limits (HEL's) for the wrought and the AM+Rx samples but a slightly higher HEL for the AM material which is consistent with the quasi-static observations of higher flow stress, as seen in the loading portion of the profile, 2) non-constant responses upon reaching the peak stress on the Hugoniot suggestive of non-uniform plastic deformation within the samples, most evident in the AM-as-built material, 3) slightly different magnitudes (depth) of "pull-back" signals suggesting different damage nucleation and growth responses with the AM-as-built materials displaying bi-linear pull-back slopes perhaps indicative of differing energy partitioning during nucleation and growth of damage as compared to the AM+Rx and wrought displaying a linear "pull-back" signal, and 4) the AM-as-built displays a shifted time interval of the "pull-back" signal reload peak consistent with the evolved damage in the sample not located solely near the center line of the sample, thereby altering the "ringing" interval in the pull-back signal, in contrast to the wrought and AM+Rx samples where the incipient damage is both concentrated and centered near the mid-plane of the sample.

In the spall experiment with a peak shock stress of 6.5 GPa, the wave profiles display some similarities and differences compared to the experiment with a 4.7 GPa peak stress, specifically: 1) the HEL's are essentially identical for all three samples, 2) the profiles are "flatter" upon attaining the peak stress level suggesting the higher peak stress was sufficient to activate more uniform plasticity in all the samples, 3) all three materials display a single slope "pull-back" signal suggesting more kinetically uniform nucleation and growth of damage between the samples, and finally 4) the AM-as-built ringing is aligned with the other two materials signaling damage evolution for all three materials is concentrated in the center of the targets.

The associated quantitative pullback and spall strength data is presented in Table II. The spall strengths between the three materials shocked to 4.7 GPa peak stress exhibit significant differences, 2.57 to 3.43 GPa. Specifically, the spall strength for the AM+Rx material is 16% higher than the AM and 25% higher than the wrought material. However, this difference in their spall strengths contracts to a range of 2.29 to 2.64 GPa at the higher peak stress, with the spall

strengths of the wrought and AM+Rx becoming statistically equal. It is interesting to note that increasing the peak stress to 6.5 GPa results in a ~ 20% decrease in the spall strength of the AM-as-built, 25% decrease in the AM+Rx, while the spall strength of the wrought material remains unchanged.

In addition, differences are also observed in the rate at which the u_{fs} traces exhibit 1) reach the minima ($\dot{u}_1$) and 2) rise beyond the minima ($\dot{u}_2$), as listed in Table II. For the 4.7 GPa peak stress, AM and AM+Rx have approximately similar release rates as compared to the wrought, which has a 8% higher release rate. The release rate can affect the nominal material volume that is pulled into tension during spall. A slower release rate, as is the case for the wrought, would normally be associated with a broader damage region. In addition, the rate of increase in the u_{fs} data beyond the minima is the highest for AM+Rx. Specifically, it is 47% higher than wrought and initially 74% higher than AM until the slopes for both become equal during later times. In single-phase, brittle and ductile materials, it has been shown that the rate at which the velocity rises can be directly correlated to rate of void growth. A higher slope in the rise of the data to the spall peak can be correlated with a higher void growth rate. For the 6.5 GPa stress, the release rates for all the samples are approximately similar whereas the rise times are different. AM experiences the highest rise time, followed by wrought and AM+Rx. Specifically, the rise time for AM is 12% higher than wrought and 28% higher than AM+Rx.

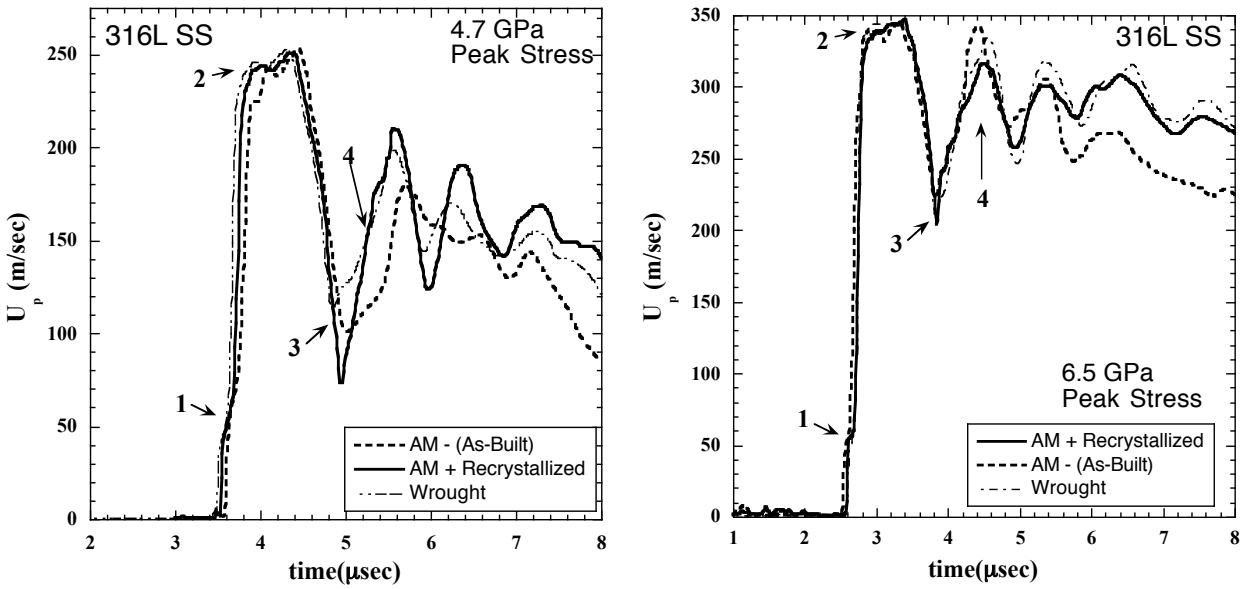

Fig. 5. PDV wave profiles (particle velocity versus time plots) for the three 316L SS materials impacted at peak stresses of a) 4.7 and b) 6.5 GPa.

Table II. Calculated and measured parameters from the u_{fs} data for 316L SS at 4.7 and 6.5 GPa peak stress.

316L SS Material	Peak U_p (m/s)	Peak Stress (GPa)	Δu_{fs} (m/s)	$\mathring{u}_1$ (m/s)	$\mathring{u}_2$ (m/s)	Spall Strength (GPa)

AM	126.8	4.72	143.3	313	59/237	2.87
AM Recyrstall.	127.0	4.71	172.1	316	223	3.43
Wrought	128.5	4.65	131.0	291	119	2.57
AM	172.8	6.52	114.4	340	214	2.29
AM Recrystall.	173.0	6.51	132.1	360	153	2.64
Wrought	175.0	6.44	131.5	350	188	2.58

3.3 Post-Mortem Metallographic Observations

Even though the in-situ u_{fs} measurements provide insight into the stress history of the dynamically loaded materials, these continuum level measurements can only provide limited information regarding the specific details of the operative, internal damage evolution mechanisms and their ties to the microstructure within a material. For this reason, metallographic characterization of the incipiently spalled samples was performed to quantify the relationship between damage evolution and microstructure as a function of material and shock loading condition.

All samples were cross-sectioned along the diameter, then prepared and inspected as described in Section 2.1. The spall region in the samples is clearly visible in Figs. 6 and 7 as the region with the maximum amount of voids. Damage was quantified in terms of void fraction, number of voids, and average void size using the Image J Software as described in Section 2.2. The damage evolution in the incipiently spalled (4.7 GPa) 316L SS varied between the three materials as shown by Fig. 6a. The first difference is in the position of the spall plane. In the wrought and AM+Rx, the maximum damage field is located in the center of the samples, as expected form the experiment geometry. The thickness of this spall plane is larger in the wrought sample consistent with a slower release rate as shown in Table II. Conversely, the AM-as-built material displays cracks and voids along the solidification layer boundaries (shown as fish-scales) located all over the sample, even in regions that do not develop peak tensile loads due to experimental design. This suggests a different mechanism for damage nucleation in the AM material.

Examination of these samples using higher magnification optical images highlights this difference in the damage nucleation mechanism. In the wrought sample, the damage field is comprised of disperse spherical voids evident along the length of the spall plane. Regions of coalesced voids linked by a network of shear localized plastic flow regions are readily observed. In fact, the majority of the ductile voids are associated with grain boundaries similar to past work in pure copper[50]. This observation for the wrought material is also consistent with previous studies on this material[33, 34]. Spherical voids along with jagged cracks and coalesced voids along grain boundaries are also observed in the AM+Rx sample although the width of the spall region is narrower in this sample. It is important to note that serial sectioning of the AM+Rx samples following longer chemical etching revealed residual memory of the AM chemical segregation at the solidification bands (fish-scale like structure), which the recrystallization at 1060°C for 1 hour clearly did not homogenize. Future research on 316L SS produced by AM+Rx will examine the effect of alternate heat-treatments on microstructure development. Contrary to these observations, AM-as-built, seen in Fig. 7a, displays mostly damage features with different thicknesses along layer solidification boundaries observed as the “fish-scale structure”. It is important to note that it is difficult to determine if the damaged regions in the AM sample

originated as voids, which then coalesced or cracks that grew in size. Some features have rounded tips, suggesting that they result from the coalescence of multiple boundary-nucleated voids whereas in other cases, the damage features exhibit sharp tips, hinting to the nucleation and growth of a crack. The data in Table II shows that AM has moderate spall strength along with a negligible void growth rate during the first part of the pull-back signal suggesting that perhaps latter is the dominant damage mechanism. In addition, damaged areas *are* seen to lie along boundaries that are nominally orthogonal to the shock direction. These observations together suggest the selection of damage sites based on a "weak" link argument, which is located around these solidification boundaries.

These qualitative observations are also supported by the quantitative data obtained via Image J shown in Table III. AM material had the least number of "voids" which were also the largest in size. Specifically, AM had 80% and 77% higher number voids as compared to the wrought and AM+Rx samples, respectively. These voids in the AM are 74% and 66% larger in size as compared to the wrought and AM+Rx materials. Although, as mentioned above the data suggests that there is no void nucleation per se but rather formation of cracks along weak boundaries. The area fraction of the voids was also minimum in the AM material supporting the "weak link" hypothesis.

TABLE III: The void diameter, number of voids and the total damage for the three experiments calculated using the optical micrographs in the Image J software.

316L SS Material	**Peak Stress (GPa)**	**Number of Voids**	**Average Size (μm^2)**	**Void Area Fraction**
AM	4.72	53	11765	0.983
AM Recyrstall.	4.71	227	4053	1.569
Wrought	4.65	262	3031	1.86
AM	6.52	NA	NA	NA
AM Recrystall.	6.51	NA	NA	NA
Wrought	6.44	NA	NA	NA

We postulate that once a critical number of "cracks" nucleate in the AM material to cause a stress relaxation there is no driving force for further nucleation or growth of damage. Hence, the material had the minimum amount of damage amongst all samples. However, the presence of "weak links" in the AM material much more than in the other two samples is still important to understand if an "ASTM-type" additive manufacturing certification process or generic AM-material produced specifications is ever to be developed. The following reasons could cause these solidification regions to act as preferred sites for damage 1) the fine dendritic structure present in these regions (as shown in Fig. 4) which can cause accelerated void nucleation and growth, 2) presence of ferrite in these regions and 3) presence of unconsolidated powder from the AM process. Further analysis showed that there was no evidence of evolved damage nor localized plasticity in the dendritic region and ferrite was also not present in significant quantities. Hence, it could be the presence of unconsolidated powder at these solidification boundaries that leads to the formation of weak links in the microstructure. In fact, unconsolidated powder is observed to be present in the AM samples loaded at 6.5 GPa as shown in the SEM images in Fig. 7b of the fully-spalled fracture surface, suggesting that this is not out

of the realm of possibilities. Also, the presence of cracks everywhere in the sample not just in the region of maximum tension could be due to the stochastic nature of the manufacturing process, which randomly creates regions of unconsolidated powder. Additional research needs to be performed to understand the effect of parameters used during the manufacturing process and the formation of these "weak" regions.

In contrast, the difference between the number and size of voids between the wrought and the AM+Rx samples was not significant. Wrought sample had 13% higher voids, which were 25% smaller in size as compared to AM+Rx. This suggests that in the wrought sample the damage process was nucleation dominated as compared to growth dominated in AM+Rx. This is also consistent with the higher spall strength along with the higher u_{fs} rise rate observed for AM+Rx in Table II which would make it harder to nucleate voids but easier to grow them once nucleation has occurred. This could possibly be attributed to the fact that the annealing process for the AM+Rx material did not get rid of the "solidification bands" completely. These areas as postulated above tend to act as weak sites and probably promote void growth as demonstrated by larger crack sizes in the AM material.

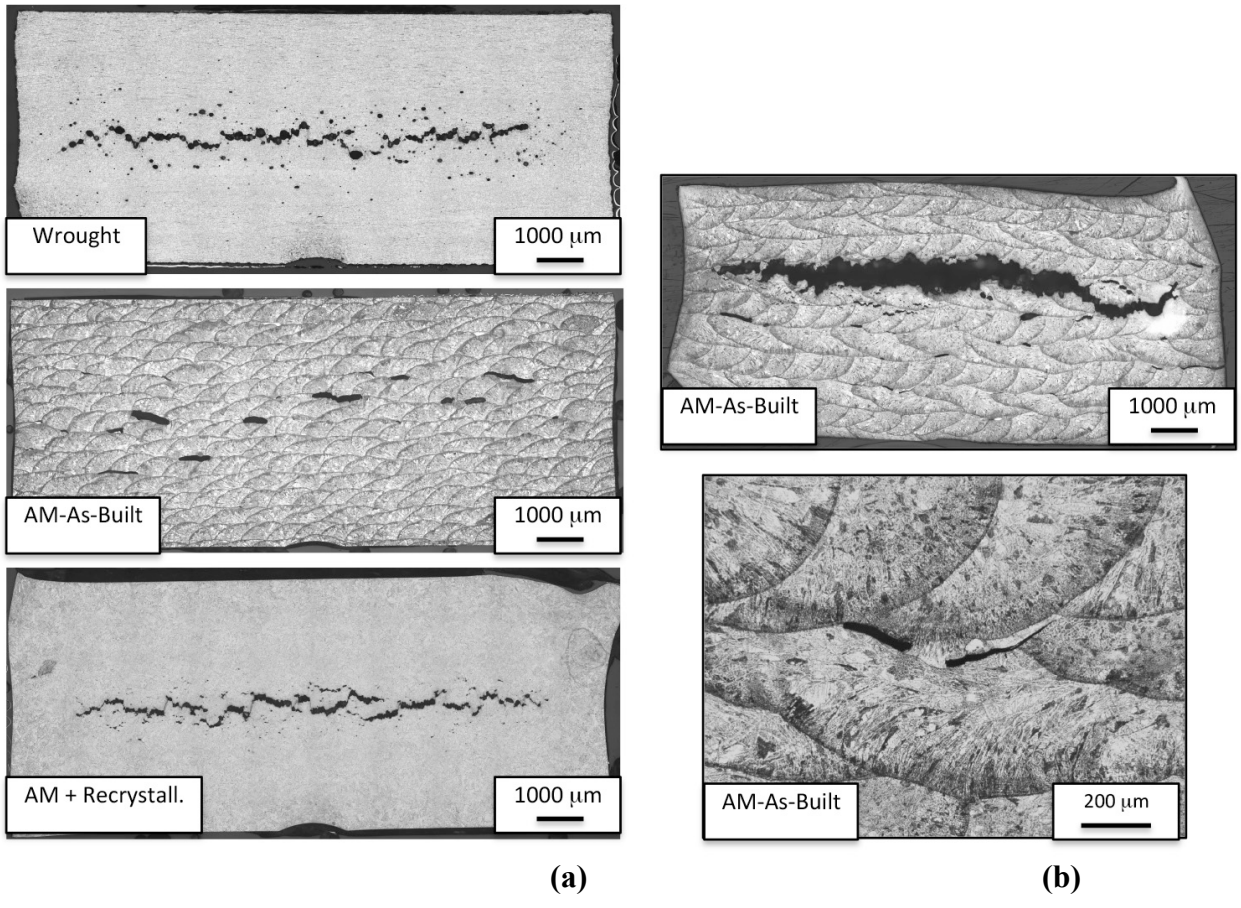

Fig. 6. Macroscopic optical metallography 316L SS in the AM-as-built condition, AM + Rx, and annealed wrought 316L SS following a) peak shock stress loading to 4.7 GPa causing incipient damage, and b) shock loading to peak stress of 6.5 GPa resulted in nearly full spall in the AM-As-Built sample and full sample fracture (complete spall) in AM-As-Built and AM+Recrystallization (details in Figure 7b).

This hypothesis is also consistent with the data obtained from the higher 6.5 GPa peak shock stress experiments. At this high stress, the samples exhibited a substantially increased level of damage evolution compared to 4.7 GPa consistent with the increased amplitude of the peak stress applied. The higher peak shock stress loading lead to complete spall fracture, i.e., a scab fractured off the rear of the sample, for the wrought and AM+Rx samples while the AM-as-built sample displayed nearly full spall fracture and stayed as one piece. Figure 6b shows the macroscopic cross-section of the nearly fully fractured AM-as-built sample and a higher magnification optical image showing preferential crack damage occurring along solidification boundaries. This is consistent with the weak link argument where after enough weak links have failed the drive for further failure is eliminated and the sample remains intact. This also agrees with the spall strength data in Table II, which shows at 6.5 GPa, the AM material had the lowest "spall" strength but the highest u_{fs} rise. Details of the full spall fracture behavior for the wrought and AM+Rx samples are presented in Figure 7b, which shows classic ductile dimpled fracture for the wrought and AM+Rx samples. This is again consistent with spherical voids nucleation, growing and coalescing at grain boundaries as seen in other classic ductile materials like copper.

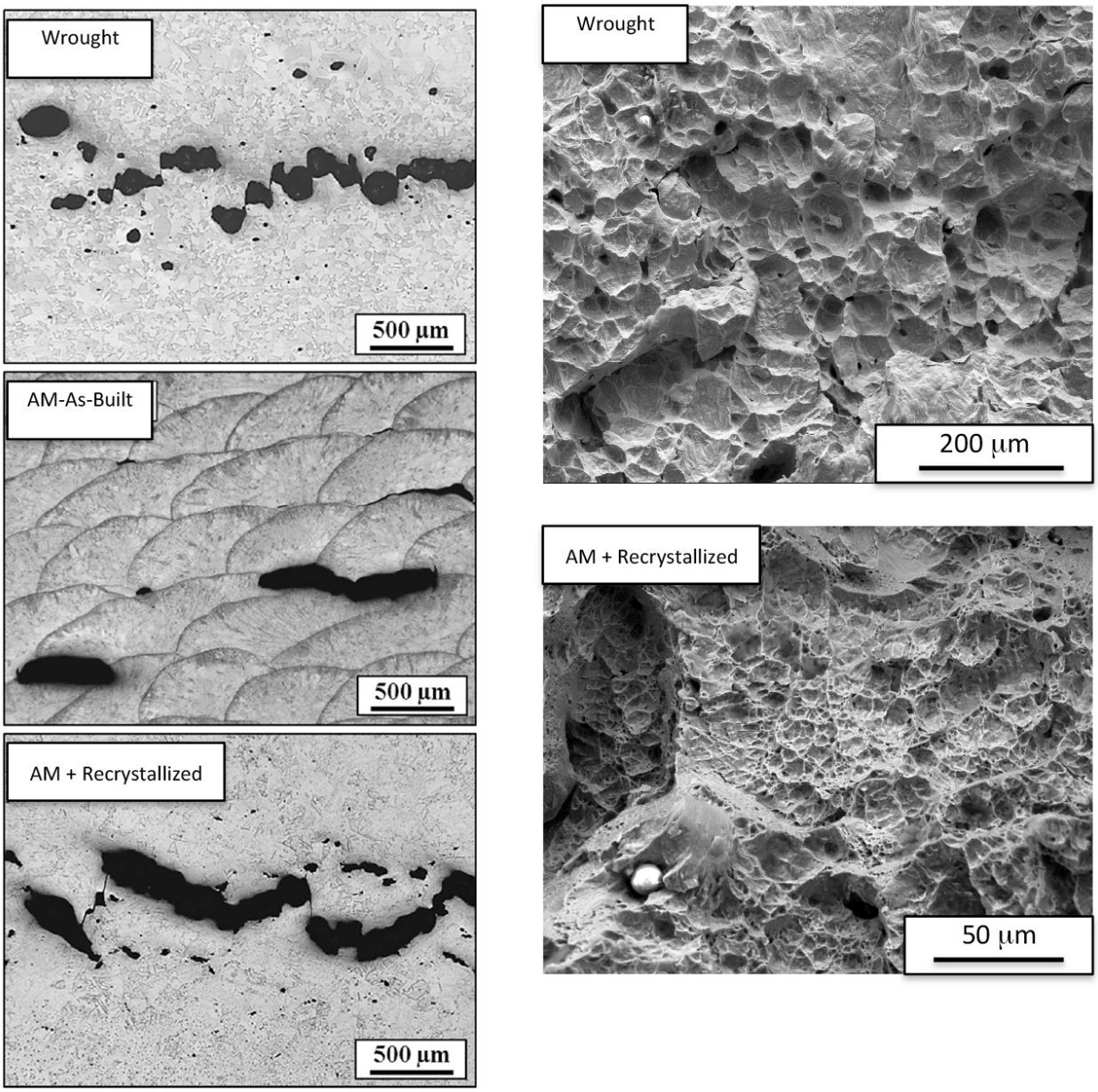

Fig. 7. (a) Higher magnification optical micrographs of damage evolution in incipiently spalled 316L SS in the AM-as-built condition, AM+Rx, and annealed wrought 316L SS following 4.7 GPa spall test, and (b) Scanning-Electron Micrographs of ductile fractures in wrought and AM + recrystallized conditions following spallation loading to 6.5 GPa.

In general, these experiments indicate that small changes during the AM process can significantly affect the material response under varying loading conditions. For example, the repeated observation of damage preferentially occurring along the solidification boundaries orthogonal to the shock-loading direction poses the question of whether this damage mode may change if the loading direction relative to the AM build direction were altered as has been demonstrated for quasi-static loading in AM-Ti-6Al-4V [27]. Previous research has demonstrated that microstructural anisotropy can significantly alter damage evolution during

spallation loading on polycrystalline wrought materials[51, 52]. Accordingly, future spallation testing of AM materials will examine how the dynamic damage evolution is affected by the orientation of loading relative to the build layer deposition direction to quantify the influence of macroscopic microstructural anisotropy known to exist in AM-as-built structures.

4. Summary and conclusions

The constitutive and shock-induced spallation response of 316L SS fabricated via directed-energy laser LENS additive manufacturing is compared to that of annealed wrought 316L SS and the AM-as-built material following recrystallization, termed AM-Rx. Results of the constitutive and dynamic spallation response of AM-as-Built, AM-Rx, and wrought 316L SS revealed:

1) The AM-as-built 316L SS displayed a 60% higher yield strength, pronounced macroscopic solidification boundary structure, and chemical segregation evident in the as-built microstructure compared to the equiaxed annealed wrought 316L SS; this increased strength believed to be due to the fine-scaled dendritic microstructure formed during solidification in the AM process. It is also important to note, that attributing the strengthening in the AM 316L SS due to residual stresses in the microstructure is not consistent with the strain-rate jump test results.
2) The AM-as-built material showed an ~10% higher spall strength when shocked to 4.7 GPa peak shock stress and ~10% lower spall strength when loaded to 6.5 GPa compared to annealed wrought 316L SS whose spall strength remained invariant for both peak shock stresses.
3) The AM 316L SS following recrystallization material displayed similar quasi-static constitutive stress-strain behavior to the annealed wrought plate but displayed differences in terms of damage evolution methodology in incipient spallation loading.
4) Preferential damage evolution in the AM-as-built material along solidification boundaries when shock-loaded orthogonal to the build direction suggests future dynamic fracture studies should probe the dynamic spall behavior of AM materials as a function of loading orientation to the build direction.

Acknowledgements

Los Alamos National Laboratory is operated by Los Alamos National Security, LLC, for the National Nuclear Security Administration of the U.S. Department of Energy under contract DE-AC52-06NA25396. This work was partially sponsored by the Joint DoD/DOE Munitions Technology Development Program.

References

[1] W.J. Sames, F.A. List, S. Pannala, R.R. DeHoff, S.S. Babu. The Metallurgy and Processing Science of Metal Additive Manufacturing, Int. Matls. Rev. 61 (2016) 315-360.

[2] W.E. Frazier. Metal Additive Manufacturing: A Review, J. Matls. Eng. and Perf. 23 (2014) 1917-1928.

[3] M. Vaezi, H. Seitz, S. Yang. A Review on 3D MIcro-Additive Manufacturing Technologies, Int. J. Adv. Manuf. Technol. 67 (2013) 1721-1754.

[4] M. Seifi, A. Salem, J. Beuth, O. Harrysson, J.J. Lewandowski. Overview of Materials Qualification Needs of Metal Additive Manufacturing, JOM 68 (2016) 747-764.

[5] Y. Zhai, D.A. Lados, J.L. Lagoy. Additive Manufacturing: Making Imagination the Major Limitation, Journal of Metals 66 (2014) 808-816.

[6] A.N. Hopkinson, P. Dickens. Analysis of rapid manufacturing – using layer manufacturing processes for production, J. Mechanical Engineering Science 217 (2003) 31-39.

[7] B.R. Berger. Additive Manufacturing: A Game Changer for the Manufacturing Industry?, Berger STrategy Consultants, Munich, Germany, 2013.

[8] T.J. Horn, O.A. Harrysson. Overview of Current Additive Manufacturing Technologies and Selected Applications, Science Progress 95 (2012) 255-282.

[9] I. Gibson, D.W. Rosen, B. Stucker. Additive Manufacturing Technologies: Rapid Prototyping to Direct Manufacturing, Springer, New York, 2010.

[10] W. Hofmeister, M.L. Griffith, M. Ensz, J. Smugeresky. Solidification in direct metal deposition by LENS processing, JOM; Journal of the Minerals, Metals, and Materials Society 53 (2001) 30-34.

[11] M.L. Griffith, M.E. Schlienger, L.D. Harwell, M.S. Oliver, M.D. Baldwin, M. Ensz, M. Essien, J. Brooks, C.V. Robino, J. Smugeresky. Understanding thermal behavior in the LENS process, Materials and Design 20 (1999) 107-113.

[12] M.L. Griffith, L.D. Harwell, J.T. Romero, M.E. Schlienger, C.L. Atwood, J. Smugeresky. Multi-Material Processing by LENS (TM). In: Bourell DL, Beaman JJ, Crawford RH, Marcus HL, Barlow JW, (Eds.). 8th Solid Freeform Fabrication (SFF) Symposium. Univ. of Texas, Ausitn, TX: Univ. of Texas Austin, Mech. Eng. Dept., Austin, TX, 1997. p.387-393.

[13] J.O. Milewski, G.K. Lewis, D.J. Thoma, G.I. Keel, R.B. Nemec, R.A. Reinert. Directed Light Fabrication of a Solid Metal Hemisphere using 5-Axis Powder Deposition, J. Matls. Proc. Tech. 75 (1998) 165-172.

[14] J.O. Milewski, D.J. Thoma, J.C. Fonseca, G.K. Lewis. Development of a near net shape processing method for rhenium using directed light fabrication, Matls. and Manuf. Processes 13 (1998) 719-730.

[15] D.L. Bourell, M.C. Leu, D.W. Rosen. Roadmap for Additive Manufacturing: Identifying the Future of Freeform Processing, University of Texas at Austin, Austin, TX, 2009.

[16] T. Foresight Project. The Future of Manufacturing: A New Era of Opportunity and Challenges for the UK. London, England, 2013.

[17] T. Energetics Incorporated. Measurement Science Roadmap for Metal-Based Additive Manufacturing. Washington, DC, 2013.

[18] N.R. Council. 3D Printing in Space, The National Academy Press, Washington, DC 20001, 2014.

[19] R. Fadida, D. Rittel, A. Shirizly. Dynamic Mechanical Behavior of Additively Manufactured Ti6Al4V with Controlled Voids, J. Appl. Mech. 82 (2015) 041004.

[20] D.R. Jones, S.J. Fensin, O. Dippo, R.A. Beal, V. Livescu, D.T. Martinez, C.P. Trujillo, J.N. Florando, M. Kumar, G.T. Gray III. Spall Fracture in Additive Manufactured Ti-6Al-4V, J. Appl. Physics 120 (2016) 135902-135901 to 135902-135908.

[21] E. Yasa, J. Deckers, J.-P. Kruth, M. Rombouts, J. Luyten. CHarpy Impact Testing of Metallic Selective Laser Melting Parts, VIrtual and Physical Prototyping 5 (2010) 89-98.

[22] B. Verlee, T. Dormal, J. Lecomte-BEckers. Density and porosity control of sinteredt 316L stainless steel parts produced by additive manufacturing, Powder Metallurgy 55 (2012) 260-267.

[23] J.A. Cherry, H.M. Davies, S. Mehmood, N.P. Lavery, S.G.R. Brown, J. Sienz. Investigation in the effect of process parameters on microstructural and physical properties of 316L stainless steel parts by selective laser melting, International journal of Advanced Manufacturing Technology 76 (2015) 869-879.

[24] A.S. Wu, D.W. Brown, M. Kumar, G.F. Gallegos, W.E. King. An Experimental Investigation into Additive Manufacturing Induced Residual Stresses in 316L Stainless Steel, Metallurgical and Materials Transactions A 45A (2014) 6260-6270.

[25] B. Zhang, L. Dembinski, C. COddet. The study of the laser parameters and environment variables effect on mechanical properties of high compact parts elaborated by selective laser melting 316L powder, Mater. Sci. Eng. A584 (2013) 21-31.

[26] H.D. Carlton, A. Haboub, G.F. Gallegos, D.Y. Parkinson, A.A. MacDowell. Damage evolution and failure mechanisms in additively manufactured stainless steel, Mater. Sci. Eng. A 651 (2016) 406-414.

[27] J.S. Keist, T.A. Palmer. Role of geometry on properties of additively manufactured Ti-6Al-4V structures fabricated using laser based directed energy deposition, Materials and Design 106 (2016) 482-494.

[28] E. Brandl, U. Heckenberger, V. Holzinger, D. Buchbinder. Additive Manufactured AISI 10Mg Samples using Selective Laser Melting, Materials and Design 34 (2012) 159-169.

[29] B. Baufeld, E. Brandl, O. van der Biest. Wire Based Additive Layer Manufacturing: Comparison of Microstructure and Mechanical Properties of Ti-6Al-4V components fabricated by laser-beam deposition and shaped metal deposition, Journal of Materials Process Technology 211 (2011) 1146-1158.

[30] V.L. G.T. Gray III, P.A. Rigg, C.P. Trujillo, C.M. Cady, S.R. Chen, J.S. Carpenter, T.J. Lienert, S. Fensin. Structure / Property (Constitutive and Dynamic Strength / Damage) Characterization of Additively Manufactured 316L SS, The European Physical Journal 94 (2015) 02006.

[31] G.T. Gray III. High-Strain-Rate Deformation: Mechanical Behavior and Deformation Substructures Induced, Annual Review of Materials Research, Vol 42 42 (2012) 285-303.

[32] S.I. Wright, B.L. Adams, K. Kunze. Application of a new automatic lattice orientation measurement technique to polycrystalline aluminum, Materials Science and Engineering A160 (1993) 229-240.

[33] G.T. Gray III, N.K. Bourne, B.L. Henrie, J.C.F. Millett. Influence of shock-wave profile shape (triangular - "Taylor-wave" versus square-topped) on the spallation response of 316L stainless steel, J. Phys. IV France 110 (2003) 773-778.

[34] G.T. Gray III, N.K. Bourne, B.L. Henrie. On the influence of loading profile upon the tensile failure of stainless steel, J. Appl. Phys. 101 (2007) 093507.

[35] J.A. Brooks, J.C. Williams, A.W. Thompson. Trends in Welding Research, ASM, 1982.

[36] C.A. Schneider, W.S. Rasband, K.W. Eliceiri. NIH IMage to IMage J: 25 Years of Image Analysis, Nature Methods 9 (2012) 671-675.

[37] G.T. Gray III. Classic Split-Hopkinson Pressure Bar Testing. ASM Handbook - Mechanical Testing and Evaluation, vol. 8. ASM International, Materials Park, OH, 2000. pp. 462-476.

[38] G.T. Gray III. Shock wave testing of ductile materials. in: Kuhn H, Medlin D, (Eds.). ASM Handbook. Vol. 8: Mechanical Testing and Evaluation. ASM International, Materials Park, Ohio, 2000. pp. 530-538.

[39] O.T. Strand, D.R. Goosman, C. Martinez, T.L. Whitworth, W.W. Kuhlow. Compact system for high-speed velocimetry using heterodyne techniques, Rev. Sci. Instrum. 77 (2006) 083108.

[40] B.J. Jensen, D.B. Holtkamp, P.A. Rigg, D.H. Dolan. Accuracy limits and window corrections for photon Doppler velocimetry, J. Appl. Phys. 101 (2007) 013523.

[41] P.S. Follansbee. Fundamentals of Strength, John Wiley & Sons, Inc., Hoboken , N.J., 2014.

[42] P. Rangaswamy, M.L. Griffith, M.B. Prime, T.M. Holden, R.B. Rogge, J.M. Edwards, R.J. Sebring. Residual stresses in LENS (R) components using neutron diffraction and contour method, Mater. Sci. Eng. A 399 (2005) 72-83.

[43] P. Rangaswamy, T.M. Holden, R.B. Rogge, M.L. Griffith. Residual stresses in components formed by the laser-engineered net shaping (LENS (R)) process, J. Strain Analysis for Engineering Design 38 (2003) 519-527.

[44] B.P. Kashyap, K. Tangri. On the Hall-Petch Relationship and Substructural Evolution in Type 316L Stainless Steel, Acta Metall. Mater. 43 (1995) 3971-3981.

[45] S.I. Wright, D.P. Field, D.J. Dingley. Advanced Software Capabilities for Automated EBSD. in: Schwartz AJ, Kumar M, Adams BL, (Eds.). Electron Backscatter Diffraction in Materials Science. Kluwer Academic / Plenum Publishers, New York, N.Y., 2000. pp. 141-152.

[46] M.C. Flemings. Solidification Processing, McGraw-Hill, New York, NY, 1974.

[47] S. Katayama, A. Matsunawa. Solidification Microstructure of Laser Welded Stainless Steels. ICALEO 1984. Boston, MA: Laser Institute of America, 1984. p.60-67.

[48] Y. Nakao, K. Nishimoto, W. Zhang. Effects of Rapid Solidification by Laser Surface Melting on Solidification Modes and Microstructures of Stainless Steels, Trans. JPN Weld Soc. 19 (1988) 20-26.

[49] G.I. Kanel. Distortion of the wave profiles in an elastoplastic body upon spalling, J. Appl. Mech. Tech. Phys. 42 (2001) 358-362.

[50] J.P. Escobedo, D. Dennis-Koller, E.K. Cerreta, B.M. Patterson, C.A. Bronkhorst, B.L. Hansen, D. Tonks, R.A. Lebensohn. Effects of grain size and boundary structure on the dynamic tensile response of copper, J. Appl. Phys. 110 (2011) 033513.

[51] G.T. Gray III, K.S. Vecchio, M.F. Lopez. Influence of Microstructural Anisotropy on the Quasi-static ad Dynamic Fracture of 1080 Eutectoid Steel. in: Staudhammer KP, Murr LE, Meyers MA, (Eds.). Fundamental Issues and Applications of Shock-Wave and High-Strain-Rate Phenomena. Elsevier Science Ltd, New York, 2001. pp. 157-163.

[52] G.T. Gray III, N.K. Bourne, K.S. Vecchio, J.C.F. Millett. Influence of anisotropy (crystallographic and microstructural) on spallation in zirconium, tantalum, HY-100 steel, and 1080 eutectoid steel, Int. J. Fract. 163 (2010) 243-258.